The Influence of Finite Conductor Thickness and Conductivity on Fundamental and Higher-Order Modes in Miniature Hybrid MIC's (MHMIC's) and MMIC's

Ke Wu, *Member, IEEE,* Rudiger Vahldieck, *Senior Member, IEEE,* Josef L. Fikart, *Senior Member, IEEE,* and H. Minkus

***Abstract*—This paper presents a rigorous analysis of the effect of finite metallization thickness and finite conductivity on the propagation characteristics of conductor-backed CPW on thin substrate. A self-consistent approach is used together with the method of lines (MoL) to determine the propagation constant, losses and field distribution of the fundamental and first two higher-order modes in CPW's with finite metallization thickness and lossy backmetallization. The method used is general and can be applied to miniature MIC's (MHMIC) and MMIC's including lossy semiconductor substrate. It is shown that the onset of higher order modes limits the usable frequency range of conductor backed CPW. The analysis includes also microstrip transmission lines on thin substrate material. It is demonstrated that a resistive strip embedded into the microstrip groundplane may potentially be useful in the design of integrated planar attenuators.**

I. Introduction

THE EFFECT of both conductor and dielectric losses in miniature hybrid MICs (MHMIC's) and monolithic MIC's (MMIC's) has received considerable attention in recent years. The main concern is with the propagation characteristics of planar transmission lines and how they behave when material parameters are less than ideal and when the conductor thickness is in the order of the skin depth. The analysis of this problem is not only very important for the design of (monolithic) microwave integrated circuits but also in the context of economical wafer utilization and hence in view of maximum circuit density [1].

Coplanar waveguides (CPW) and microstrip transmission lines are the main building blocks for MHMIC's and MMIC's. Because of the small circuit dimensions, the mode propagation in both transmission lines is strongly influenced by nonideal material parameters. Furthermore, assuming CPW's as uniplanar transmission lines may not be a realistic assumption in a practical circuit environment where the metallic housing of the final chip or the mounting jig is normally directly attached to the opposite side of the transmission line substrate and thus represents a backmetallization. Hence, accurate modelling of CPW's must not only include losses introduced by the conductor and dielectric, but also the effect of a backmetallization as well as its losses. The latter point is in particular of interest in the case of CPW's and microstrip lines on thin substrate, ≤10 mils.

To determine transmission line losses, the value of commonly used perturbation methods [2]–[6] or Wheeler's incremental inductance rule become questionable in light of the fact that the miniaturized dimensions are not always large in comparison with the skin depth. Also, due to the thin substrate thickness and the close vicinity of the back metallization (CPW) to the center conductor, quasi-TEM mode propagation cannot always be guaranteed. In particular on miniaturized CPW's, higher-order modes may propagate along with the quasi-TEM wave. Therefore, it is important to use a full wave approach to account for higher order mode effects. So far, only a few comprehensive approaches were proposed [7]–[12]. However, most of these papers treat only relatively simple strip geometries assuming quasi-TEM modelling on the basis of extended equivalent or static models. Furthermore, in most of these papers the overall losses are calculated as a linear superposition of dielectric losses and conductor losses. Strictly speaking, this can only be viewed as a first order approximation because the field equations contain the loss factors in a nonlinear fashion. Among the different methods that have been developed in the past, the self-consistent description of metallic losses, which describes the metallic layer as lossy dielectric, together with the mode matching method [13], [14] were most promising. This research had shown that contrary to the traditional perception the propagation constant in a microstrip at low frequencies and under the influence of a lossy conductor, shows a negative slope versus frequency. These theoretical results have not only been confirmed in a recent experiment [17] but also by the theoretical results given in this paper.

Since the mode matching method is known for its relative convergence behavior [13], [14] as well as its limited capability to model arbitrary circuit contours, we adopted the self-consistent approach for the MoL [15] at approximately the same time as the authors in [16]. The MoL is not subject to the same limitations as the mode matching method and

Manuscript received December 17, 1991; revised June 30, 1992.

K. Wu is with the Department of Electrical and Computer Engineering, Ecole Polytechnique de Montreal, Montreal, PQ Canada.

R. Vahldieck is with the Department of Electrical and Computer Engineering, P.O. Box 3055, University of Victoria, Victoria, BC, Canada V8W 3PC.

J. L. Fikart and H. Minkus are with MPR Teltech Ltd., Microwave Division, 8999 Nelson Way, Burnaby, BC V5A 4B5.

IEEE Log Number 9205451.

is more flexible for the analysis of arbitrarily shaped circuit contours. In contrast to [16], the analysis presented here includes also higher-order modes and therefore goes beyond the work presented in [15] and [16]. The algorithm described in this paper can equally be applied to slotlines, microstrip lines and CPW's on lossy semiconductor (multilayered) substrate. Of particular interest is the field distribution of the fundamental and two first higher-order modes. This knowledge may help to better understand the mode conversion problem usually responsible for the upper frequency limit in a conductor backed CPW.

Besides analyzing the general influence of conductor losses, this paper investigates also the effect of a high or low conductive strip embedded into the groundplane (microstrip) or backmetallization (CPW). While a highly conductive strip leads to lower overall losses, in particular for transmission lines with very thin substrate material, a resistive strip in the groundplane of a microstrip line may potentially be useful to built planar attenuators. Such a structure has not been investigated yet.

II. Method of Analysis

In the self-consistent approach the lossy conductor area is treated as an ordinary lossy dielectric region which is characterized by its complex dielectric permittivity. The imaginary part of this complex value is usually very high because it represents the conductivity of the material used.

The transmission line cross-section can be regarded as multilayered dielectric structure with inhomogeneous subregions. With reference to the example displayed in Fig. 1, the first layer is a protecting layer (i.e. SiN_3) while the second layer represents a region of coupled multiconductors with finite conductivity. Since the groundplane is an imperfect conductor on the backside of the supporting substrate (alumina or GaAs), but usually thicker than the strips on the substrate surface and also thicker than the skin depth, a skin-effect layer is assumed as an additional layer with finite conductivity σ_g. The thickness of this layer equals the skin depth:

$$t_5 = \delta = \sqrt{\frac{2}{\omega\mu_0\sigma_g}}. \tag{1}$$

The properties and advantages of the method of lines have been well described in [19]–[21]. Therefore, the following paragraphs focus only on the principal analytical formulations. Within the inhomogeneous layer (Fig. 1, t_2 and t_3) the dielectric permittivity $\epsilon(x)$ changes abruptly. Hence, the electromagnetic field for each electric and magnetic discretization line is expressed as a superposition of LSM/LSE potential functions rather than TE/TM potential functions [21], [22]. Based on the argument in [21], a magnetic line is placed into the dielectric interface to meet the boundary condition (Fig. 2). However, since an inhomogeneous discretization scheme is used in this paper, the average value of dielectric permittivity at the interface between two adjacent subregions, as given in [21], is no longer valid and a more generalized formulation for this value is used (see Appendix).

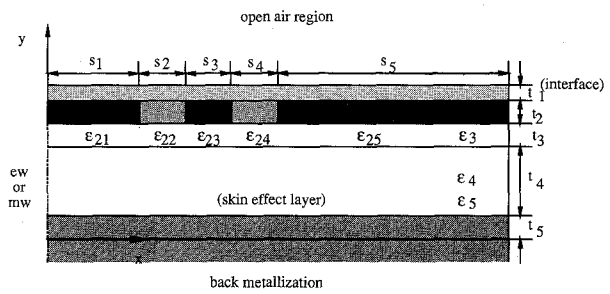

Fig. 1. Cross-section of the CPW illustrating finite metallization thickness.

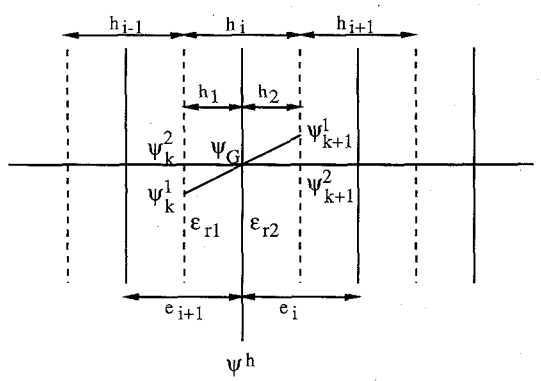

Fig. 2. Inhomogeneous discretization scheme at the abrupt dielectric/conductor interface.

A. Theory

The electromagnetic field components are derived from two independent LSM/LSE vector potential functions:

$$\vec{E} = \frac{1}{j\omega\epsilon_0\epsilon_r(x)}\nabla\times\nabla\times(\psi^e\vec{e}_x) - \nabla\times(\psi^h\vec{e}_x)$$
$$\vec{H} = \nabla\times(\psi^e\vec{e}_x) + \frac{1}{j\omega\mu}\nabla\times\nabla\times(\psi^h\vec{e}_x). \tag{2}$$

For transmission line problems the potential functions are expressed as

$$\psi^{e,h}(x,y,z) = \psi^{e,h}(x,y)\exp(-\gamma z) \tag{3}$$

where γ is the unknown complex propagation constant, and e, h denote the LSM and LSE modes, respectively. The scalar functions ψ^e and ψ^h must fulfill the Helmholtz and Sturm-Liouville equations:

$$\frac{\partial^2\psi^h}{\partial y^2} + \frac{\partial^2\psi^h}{\partial x^2} + (\epsilon_r(x)k_0^2 - \gamma^2)\psi^h = 0$$
$$\frac{\partial^2\psi^e}{\partial y^2} + \epsilon_r(x)\frac{\partial}{\partial x}\left(\frac{1}{\epsilon_r(x)}\frac{\partial\psi^e}{\partial x}\right) + (\epsilon_r(x)k_0^2 - \gamma^2)\psi^e = 0 \tag{4}$$

with $k_0^2 = \omega^2\mu_0\epsilon_0$.

By applying the results presented in [23] (in order to obtain symmetry of the elementary matrices), normalized potential functions are used in case of the inhomogeneous discretisation:

$$\vec{\phi}^{e,h} = [r_{e,h}]^{-1}\vec{\psi}^{e,h}$$
$$[r_{e,h}] = \mathrm{diag}\left(\sqrt{\frac{h_0}{e_i, h_i}}\right) \tag{5}$$

with the limiting discretisation size h_0. As a consequence of shifting between the e and h lines (refer to [23]), the size of the intervals intersected by the discretization lines for e and h are denoted by $e_i (i = 1, 2, \cdots, N^e)$ and $h_i (i = 1, 2, \cdots, N^h)$, respectively. For the inhomogeneous layer, the dielectric permittivity is expressed as diagonal matrices:

$$\begin{aligned} \epsilon_r(x) &\xrightarrow{e\text{-lines}} \operatorname{diag}(\epsilon_r(x)) = [\epsilon_r^e] \\ \epsilon_r(x) &\xrightarrow{h\text{-lines}} \operatorname{diag}(\epsilon_r(x)) = [\epsilon_r^h] \end{aligned} \tag{6}$$

The first-order finite difference expressions for the first and second derivatives of ψ^e and ψ^h with respect to x can be written as follows:

$$\begin{aligned} &[r_e]^{-1}\left(h_0\frac{\partial\vec{\psi}^h}{\partial x}\right) \rightarrow [D_x]\vec{\phi}^h \\ &[r_h]^{-1}\left(h_0\frac{\partial\vec{\psi}^e}{\partial x}\right) \rightarrow -[D_x]^t\vec{\phi}^e \\ &[r_h]^{-1}\left(h_0^2\frac{\partial^2\vec{\psi}^h}{\partial x^2}\right) \rightarrow -[D_x]^t[D_x]\vec{\phi}^h \\ &[r_e]^{-1}\left(h_0^2\frac{\partial^2\vec{\psi}^e}{\partial x^2}\right) \rightarrow \\ &\quad -[D_x][D_x]^t\vec{\phi}^e \text{ (homogeneous layers)} \\ &[r_e]^{-1}\left(h_0^2\epsilon_r(x)\frac{\partial}{\partial x}\left(\frac{1}{\epsilon_r(x)}\frac{\partial\vec{\psi}^e}{\partial x}\right)\right) \rightarrow \\ &\quad -[\epsilon^e][D_x][\epsilon^h]^{-1}[D_x]^t\vec{\phi}^e \text{ (inhomogeneous layers)} \end{aligned} \tag{7}$$

Using the transformation matrices T^e and T^h, the normalized potential function vectors are transformed into $\vec{V}^e$ and $\vec{V}^h$ by the following relationship:

$$\vec{\phi}^{e,h} = \begin{cases} T^{e,h}\vec{V}^{e,h} & \text{(homogeneous layers)} \\ T^{e,h}P^{e,h}\vec{V}^{e,h} & \text{(inhomogeneous layers)} \end{cases} \tag{8}$$

in which a complex $P^{e,h}$ eigenvector for the inhomogeneous layer is added. Note that the transformation matrices T have orthogonal property. As a result, the Helmholtz and Sturm-Liouville differential equations are now written in the transformed domain:

$$\frac{d^2\vec{V}^{e,h}}{dy^2} - [k^{e,h}]^2\vec{V}^{e,h} = 0 \tag{9}$$

with (10) shown at the bottom of the page. Here the elementary matrices are

$$\begin{aligned} [\xi] &= [T^e]^t[D_x][T^h] \\ [\tilde{\epsilon}^e] &= [T^e]^t[\epsilon_r^e][T^e] \\ [\tilde{\epsilon}^h] &= [T^h]^t[\epsilon_r^h][T^h] \end{aligned} \tag{11}$$

where P is determined by the QR algorithm in such a way that $P^{-1}(\cdots)P$ is diagonalized. The resulting decoupled ordinary differential equations takes the form of simple wave equations:

$$\begin{bmatrix} \vec{V}^{e,h} \\ \dfrac{d\vec{V}^{e,h}}{dy} \end{bmatrix}_{y_2} = \underbrace{\begin{bmatrix} [\cos k^{e,h}(y_2 - y_1)] & \left[\dfrac{\sin k^{e,h}(y_2 - y_1)}{k^{e,h}}\right] \\ k^{e,h}\sin k^{e,h}(y_2 - y_1) & [\cos k^{e,h}(y_2 - y_1)] \end{bmatrix}}_{Q^{e,h}} \begin{bmatrix} \vec{V}^{e,h} \\ \dfrac{d\vec{V}^{e,h}}{dy} \end{bmatrix}_{y_1} \tag{12}$$

in which the submatrices are diagonal. $Q^{e,h}$ is a dual transmission line matrix that establishes a direct link between the boundary conditions from $y = y_1$ to $y = y_2$.

Through (2), the field quantities can be derived in terms of the electric and magnetic potential functions. By substituting the previously discussed relationships regarding the transformation of the potential functions into these expressions, a set of tangential field components in the discrete transformed domain is obtained in (13) at the bottom of the next page. This is a generalized interface matrix between the field components and the potential functions, in which $P^{e,h}$ and $[\tilde{\epsilon}^{e,h}]$ are reduced to the identity matrix and a scalar value when homogeneous layers are considered.

The field continuity conditions between interfaces leads to a cascaded multiplication of matrices R and Q:

$$\begin{pmatrix} j\tilde{e}_x \\ \tilde{e}_x \\ \tilde{h}_z \\ j\tilde{h}_x \end{pmatrix}_{\text{interface}^-} = \left(\prod_{i=1}^{i=4} R_i Q_i R_i^{-1}\right) R_5 Q_5 \begin{pmatrix} \vec{V}^e \\ \dfrac{d\vec{V}^e}{dy} \\ \vec{V}^h \\ \dfrac{d\vec{V}^h}{dy} \end{pmatrix}_{\text{bottom plane}} \tag{14}$$

$$[k^e] = \begin{cases} \sqrt{\dfrac{[\xi][\xi]^t}{h_0^2} - \epsilon_r k_0^2 - \gamma^2} & \text{(homogeneous layers)} \\ \sqrt{P^{e^{-1}}\left(\dfrac{[\tilde{\epsilon}^e][\xi][\tilde{\epsilon}^h][\xi]^t}{h_0^2} - [\tilde{\epsilon}^e]k_0^2\right)P^e - \gamma^2} & \text{(inhomogeneous layers)} \end{cases}$$

$$[k^h] = \begin{cases} \sqrt{\dfrac{[\xi]^t[\xi]}{h_0^2} - \epsilon_r k_0^2 - \gamma^2} & \text{(homogeneous layers)} \\ \sqrt{P^{h^{-1}}\left(\dfrac{[\xi]^t[\xi]}{h_0^2} - [\tilde{\epsilon}^h]k_0^2\right)P^h - \gamma^2} & \text{(inhomogeneous layers)} \end{cases} \tag{10}$$

and

$$\begin{pmatrix} j\tilde{e}_x \\ \tilde{e}_z \\ \tilde{h}_z \\ j\tilde{h}_x \end{pmatrix}_{\text{interface}^+} = R_{\text{air}} Q_{\text{air}} \begin{pmatrix} \vec{V}^e \\ \dfrac{d\vec{V}^e}{dy} \\ \vec{V}^h \\ \dfrac{d\vec{V}^h}{dy} \end{pmatrix}_{\text{cover}} \tag{15}$$

with

$$Q = \begin{pmatrix} Q^e & 0 \\ 0 & Q^h \end{pmatrix}. \tag{16}$$

It is worthwhile noting that removing the top cover to infinity is straightforward by introducing the open air impedances/admittances for the LSE (Y) and LSM (Z) modes in (15). This leads to a matrix product of the following form for the vector at the right hand side of (15):

$$\begin{pmatrix} 1 & 0 & 0 & 0 \\ 0 & Y^e & 0 & 0 \\ 0 & 0 & 1 & 0 \\ 0 & 0 & 0 & Z^h \end{pmatrix} \begin{pmatrix} \vec{V}^e \\ \vec{V}^e \\ \vec{V}^h \\ \vec{V}^h \end{pmatrix}.$$

Now also half-open structures can be simulated, which is the more realistic case compared to the structures investigated in [16]. The final matrix equation system is obtained after matching the fields at the air-dielectric interface (Fig. 1) as well as applying the remaining boundary conditions at the bottom plane, and transforming the related matrices back into the original domain:

$$\begin{pmatrix} Y_{xx} & Y_{xz} \\ Y_{zx} & Y_{zz} \end{pmatrix} \begin{pmatrix} j\vec{E}_x \\ \vec{E}_z \end{pmatrix} = \begin{pmatrix} 0 \\ 0 \end{pmatrix}. \tag{17}$$

The zeros of the determinant of matrix Y yield the complex propagation constant at a given frequency for all possible modes, including higher-order modes.

In order to calculate the field components over the cross-section, the reverse procedure must be applied. First the tangential field quantities at the air-dielectric interface (Fig. 1) are calculated. To do so, the first element of the column for the electric fields in (17) is assumed to be an arbitrary constant. Starting from there, the remaining elements can be computed using the singular value decomposition or least square technique, and hence all field components at this interface can be obtained through (17). Both (14) and (15) can be regarded as excitation sources for both sides of the transverse section. Then using the transmission line matrix in the transformed domain allows to calculate the field components from layer to layer including the multiconductor region.

B. A Combining Recursive/Partitioning Technique

The previous procedure outlines in detail the formulation for the self-consistent approach to include the finite metallization thickness into the analysis. However, if these expressions are directly implemented into a computer algorithm, the hyperbolic functions (sinh and cosh) in (12) lead inevitably to large numbers, which either cause computer overflow problems or ill-conditioned matrices with problems of numerical instability. Overcoming this difficulty was a key point in the software development. To solve this problem, an artificial recursive/partitioning technique is introduced which has been successfully used in the software generating the results presented in this paper.

In explaining this approach we first examine the factor k in the argument of the hyperbolic functions. Obviously, the use of a fine discretization (small h_0) and high permittivity at low frequencies increases significantly the value of k in (10) and hence even more so the values for sinh and cosh. Therefore, to avoid overflow problems and matrix instabilities the maximum allowable value of the product k times the thickness of subregion t has to be restricted to the allowable maximum machine constant. This can be achieved by partitioning a thick layer into multiple subregions. However, subsequent multiplications to interconnect the partitioned subregions will again introduce large numbers which may exceed the range of the computer. Therefore, the following recursive technique is used instead.

After applying the boundary conditions at the bottom plane, (13) can be used to obtain a relationship between electric and magnetic fields at the interface between the 4th and 5th layer (Fig. 1):

$$\begin{pmatrix} j\tilde{h}_x \\ \tilde{h}_z \end{pmatrix}_{4,5} = \begin{pmatrix} \tilde{Z}_{xx} & \tilde{Z}_{xz} \\ \tilde{Z}_{zx} & \tilde{Z}_{zz} \end{pmatrix}_{4,5} \begin{pmatrix} j\tilde{e}_x \\ \tilde{e}_x \end{pmatrix}_{4,5}. \tag{18}$$

In this expression only the hyperbolic function tanh is used. In the absence of any metallic boundaries, the upper and lower interfaces of any other dielectric layer, including the lossy conductor layer, are linked by the following generalized matrix equation, which is shown here for the example of the interface

$$\begin{pmatrix} j\tilde{e}_x \\ \tilde{e}_z \\ \tilde{h}_z \\ j\tilde{h}_x \end{pmatrix} = \underbrace{\begin{pmatrix} \dfrac{[\tilde{\epsilon}^e]^{-1}P^e}{\omega\epsilon_0}(-\gamma^2[I]-[k^e]^2) & 0 & 0 & 0 \\ \dfrac{-j\gamma}{\omega\epsilon_0 h_0}[\tilde{\epsilon}^h]^{-1}[\xi]^t P^e & 0 & 0 & P^h \\ 0 & -P^e & +\dfrac{j\gamma}{\omega\mu h_0}[\xi]P^h & 0 \\ 0 & 0 & \dfrac{P^h}{\omega\mu}(\gamma^2[I]-[k^h]^2) & 0 \end{pmatrix}}_{R} \begin{pmatrix} \vec{V}^e \\ \dfrac{d\vec{V}^e}{dy} \\ \vec{V}^h \\ \dfrac{d\vec{V}^h}{dy} \end{pmatrix} \tag{13}$$

between layer 4 and 5 (Fig. 1):

$$\begin{pmatrix} j\tilde{e}_x \\ \tilde{e}_z \\ j\tilde{h}_x \\ \tilde{h}_z \end{pmatrix}_{3,4} = \begin{pmatrix} \tilde{Z}^{ee}_{xx} & \tilde{Z}^{ee}_{xz} & \tilde{Z}^{eh}_{xz} & \tilde{Z}^{eh}_{xz} \\ \tilde{Z}^{ee}_{zx} & \tilde{Z}^{ee}_{zz} & \tilde{Z}^{eh}_{zx} & \tilde{Z}^{eh}_{zz} \\ \tilde{Z}^{he}_{xx} & \tilde{Z}^{he}_{xz} & \tilde{Z}^{hh}_{xx} & \tilde{Z}^{hh}_{xz} \\ \tilde{Z}^{he}_{zx} & \tilde{Z}^{he}_{zz} & \tilde{Z}^{hh}_{zx} & \tilde{Z}^{hh}_{zz} \end{pmatrix} \begin{pmatrix} j\tilde{e}_x \\ \tilde{e}_z \\ j\tilde{h}_z \\ \tilde{h}_z \end{pmatrix}_{4,5}. \tag{19}$$

The matrix elements in (19) can be easily derived analytically through (13) and (16), that is RQR^{-1}. By substituting (18) for the vector on the right-hand side of (19), a similar expression as in (18) can be obtained for the interface between 3th and 4th layers. Subsequently, applying this recursive procedure from the topcover down and the bottom side up through the entire structure directly into the interface air-dielectric, leads also to the final matrix (17) without resorting to the cascaded matrix multiplication of the conventional approach, which was described first. Combining the recursive approach with the partitioning technique will improve significantly the numerical stability, in particular for thick conductors with high conductivity at low frequencies. The recursive procedure is straightforward and easy to implement on a computer. However, in conjunction with the partitioning technique the CPU-time may increase and is therefore only be used if necessary. A general rule to determine how many times a thick layer must be partitioned is given in the following:

$$N(\text{partition number}) \geq \frac{t \cdot \max\left(|k^e|, |k^h|\right)}{\ln\left(C_{\max}\right)} \tag{20}$$

where $\max |k|$ means the maximum element of the diagonal matrix k described in (10) for both e and h lines, and $C_{\max}$ is the allowable maximum machine constant which depends on the machine used.

III. Results and Discussion

In the following discussion, the quasi-lossless and very thin protecting layer on top of the conductors in Fig. 1 is not taken into account, because its influence on the propagation characteristic was found to be negligible. All conductors, including the groundplane for the CPW, are assumed to be gold with a conductivity of $\sigma_g = 3.33 \times 10^4\ (\Omega\text{mm})^{-1}$, unless otherwise specified. Because of the small center conductors used in our analysis, a non-equidistant discretization scheme has been used throughout.

Fig. 3(a) shows the dispersion diagram and losses for the fundamental and first higher-order modes for the coplanar waveguide on alumina substrate backed by a lossless metal plane. Instead of airbridges via holes are used to connect the groundplane. The distance of the via holes from the CPW slots is 1 mm. It is interesting to see that at about 23 GHz the two first higher-order modes start to propagate almost simultaneously. As a result, a substantial amount of power normally carried by the fundamental mode is now converted into one of the higher-order modes. The effect of this mode conversion is an increase of the insertion loss. This is illustrated in the measurement shown in Fig. 4(a) for a simple CPW through line. The measurement was performed using the WILTRON 360 network analyzer and the 40 GHz WILTRON

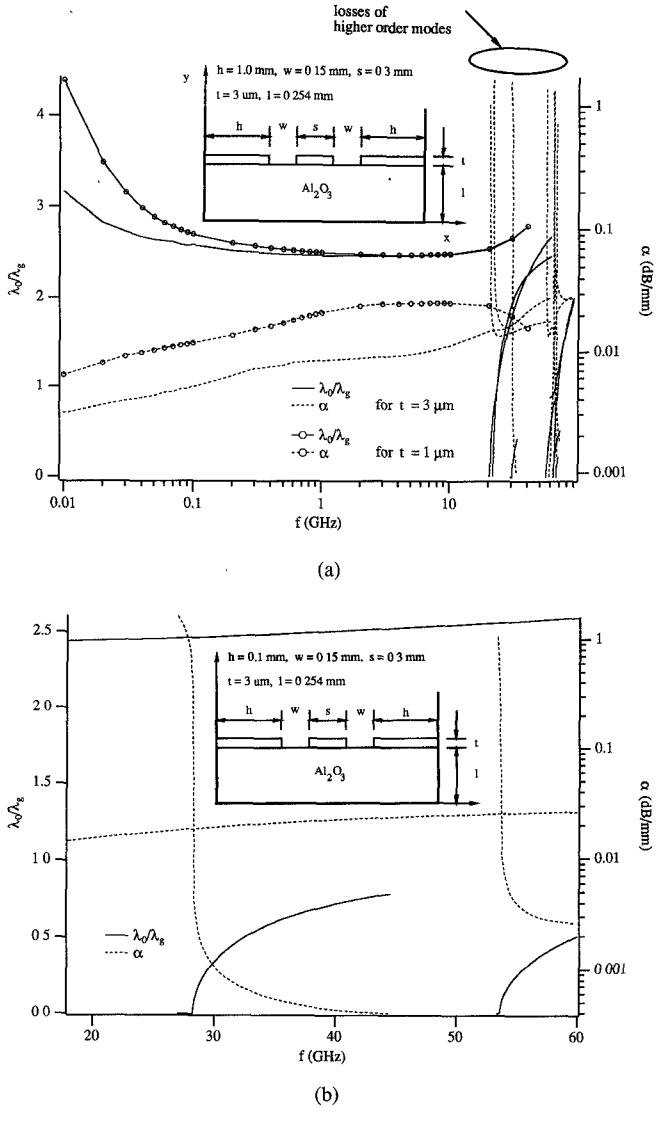

Fig. 3. (a) Dispersion and loss characteristics of fundamental and higher order modes in a CPW with via holes on alumina substrate. Distance of the via holes from the slots: $h = 1$ mm. (b) Dispersion and loss characteristics of the structure shown in Fig. 3(b) except that the via holes are now closer to the slots ($h = 0.1$ mm).

test fixture. Due to a lack of 10 mils CPW standards, the network analyzer was calibrated with 25 mils CPW standards. Furthermore, the actual length of the CPW line under test was shorter than the calibration line. Therefore, the measurement in Fig. 4(a) is only a qualitative value but sufficient to support the theoretical results of Fig. 3(a). Since higher-order modes are mainly confined in the dielectric, the via holes virtually act as waveguide sidewalls and their location determines the cutoff frequency of these modes. This is clearly shown in Fig. 3(b) where the via hole location is moved closer to the slots (0.1 mm). In this case the cutoff frequency of both modes increases beyond 54 GHz. Again, this theoretical prediction is confirmed by qualitative measurements shown in Fig. 4(b). In this case the network analyzer was calibrated with 10 mils microstrip standards, because the 25 mils CPW standard used in Fig. 4(a) could not be used for frequencies higher than 40 GHz. The importance of this measurement was to demonstrate that no higher-order modes are generated.

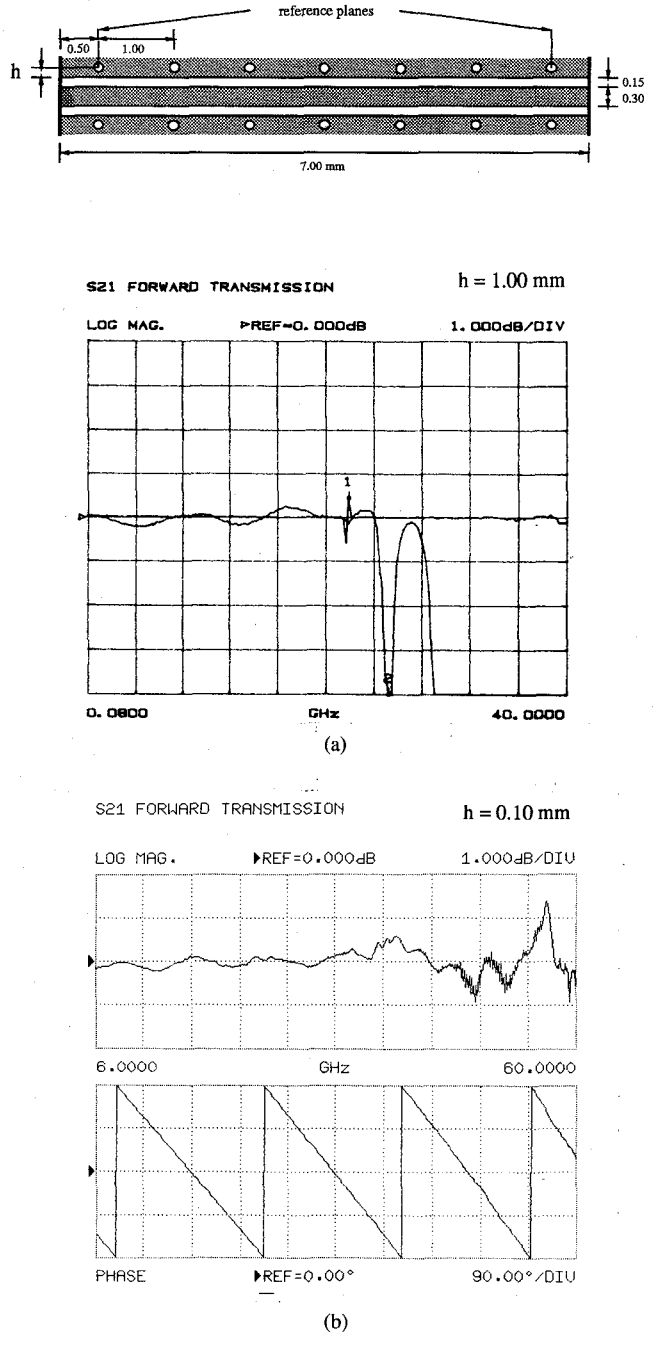

Fig. 4. (a) Measurement of S21 of the CPW through line shown in Fig. 3(a). Network analyzer was calibrated with 25 mils CPW standards (lengths of the standards 10 mm). (b) Measurement of S21 of the CPW through line shown in Fig. 3(b). New via hole location ($h = 0.1$ mm). Network analyzer was calibrated with 10 mils microstrip standards (lengths of the standards 10 mm).

Analyzing Fig. 3(a) carefully, we notice a higher-order mode at about 29 GHz, which is virtually not affected by the location of the via holes. The propagation constant of this mode remains below $\lambda o/\lambda g = 1$. which indicates that this mode could be a surface mode. It is difficult to say from the theoretical and experimental results obtained so far, to what extend this mode influences the line characteristics. If this mode is excited, it does not seem to contribute to transmission line losses, at least the measurement results do not indicate a significant effect.

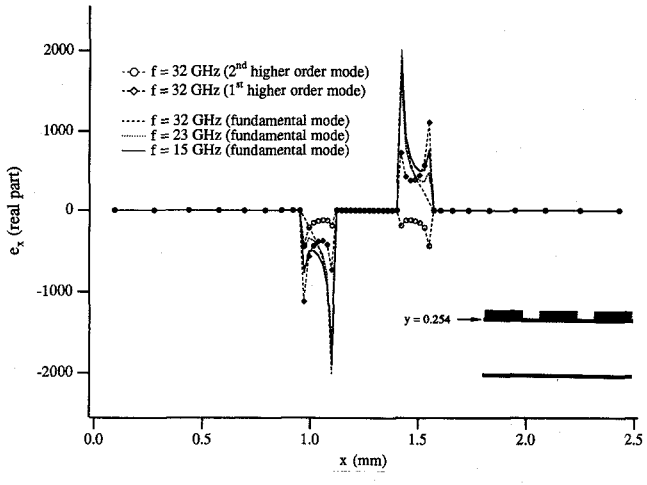

Fig. 5. Electric field (e_x) distribution (along the x-direction) for the fundamental and first two higher-order modes of the structure in Fig. 3(a) at $y = 0.254$ mm.

To gain a better understanding of the field distribution in a conductor-backed CPW, the following analysis is focused on the fundamental and two first higher-order modes at different frequencies. In this analysis the structure of Fig. 3(a) is used. Fig. 5 displays the real part of the e_x-field component of the CPW along the interface plane just between the conductors and the dielectric for different modes and different frequencies. At 15 GHz the fundamental mode behaves as expected, showing a significant field amplitude of the e_x-field at the edges of the conductor and the groundplane. At 32 GHz this e_x-field is zero at the edges of the groundplane, which indicates that the field of the fundamental mode is no longer concentrated in the slot area. At the same frequency the amplitude of the e_x-field of the first two higher-order modes is increased, indicating that they now carry more power in the slot area, which was not the case below their cutoff frequency. However, since this field orientation is incompatible with the field required in a coax launcher used in our measurement, the insertion loss increases. Fig. 6 illustrates the e_x-field half the substrate thickness below the conductor plane. The e_y-field distribution is shown in Figs. 7 and 8. As expected for the conductor-backed CPW on 10 mils substrate, at 15 GHz there is already a relatively strong e_y-field concentration below the center conductor (Fig. 8) which increases further at 32 GHz. This E-field orientation is compatible with the fundamental waveguide type mode within the substrate and therefore these modes are likely to be excited.

Besides the effect of higher-order modes there is another interesting observation to be made from the dispersion diagrams of Fig. 3, namely that the fundamental mode propagation constant exhibits a negative slope versus frequency. This fundamental mode characteristic has been reported in previous work (i.e. [13]–[15]) where finite metallization thickness and conductor losses have been taken into account. This effect has also been confirmed by measurements [17]. The negative slope of the mode is in particular obvious at lower frequencies up to 0.5 GHz. This phenomenon is probably due to the fact that below this frequency the field penetrates deeply into the conductor, which, due to its losses, behaves similar to a

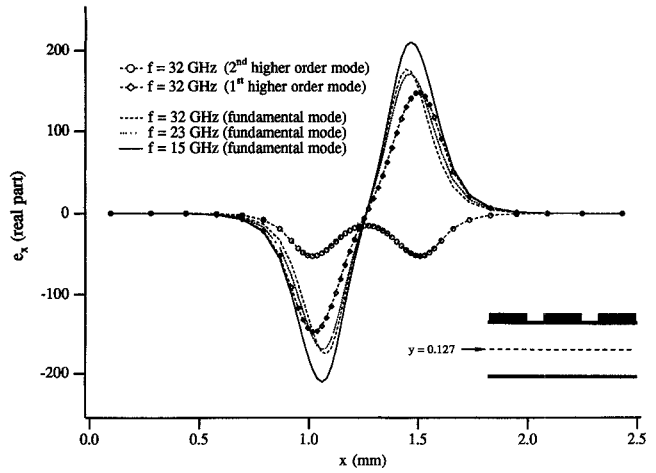

Fig. 6. Electric field (e_x) distribution (along the x-direction) for the fundamental and first two higher-order modes of the structure in Fig. 3a at $y = 0.127$ mm.

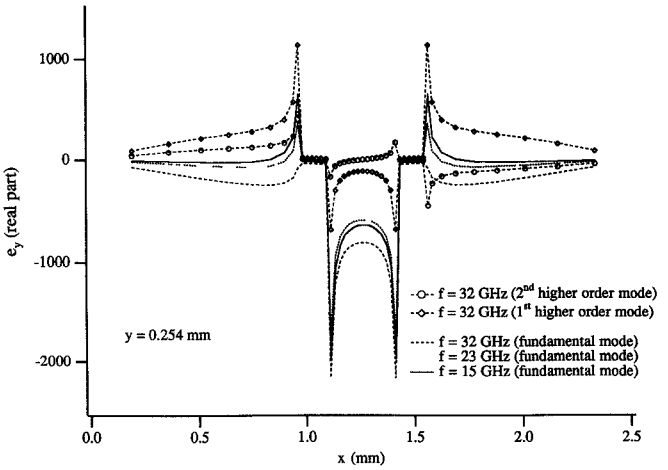

Fig. 7. Electric field (e_y) distribution (along the x-direction) for the fundamental and first two higher-order modes of the structure in Fig. 3(a) at $y = 0.254$ mm.

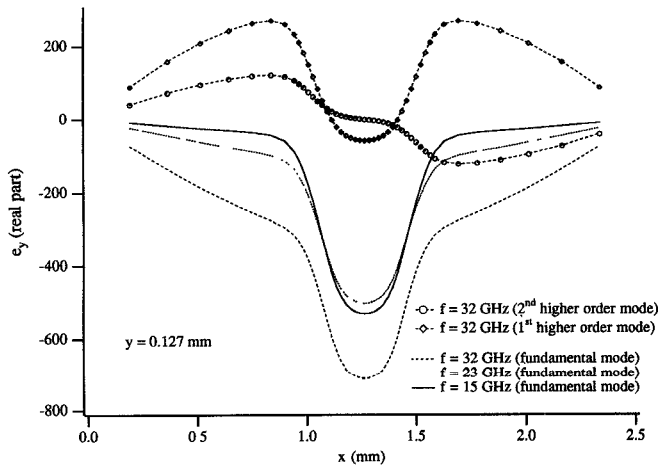

Fig. 8. Electric field (e_y) distribution (along the x-direction) for the fundamental and first two higher-order modes of the structure in Fig. 3(a) at $y = 0.127$ mm.

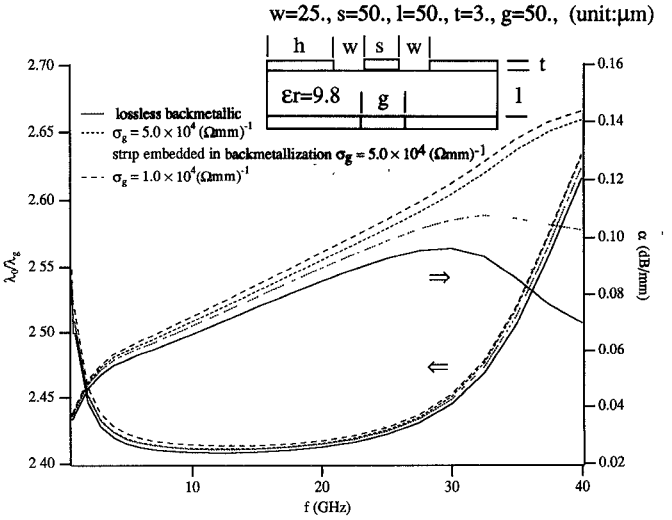

Fig. 9. Comparison of dispersion and loss characteristic of CPW on very thin substrate with different conductivity of the backmetallization, including a strip of variable conductivity embedded into the backmetallization. $h = 1$ mm.

semiconductor. Hence, the fundamental mode acts like a slow-wave mode and can therefore be explained in a similar way. Also shown in Fig. 3 is the effect of conductor thickness on the fundamental mode. For a thin conductor $(t = 1.\mu\text{m})$ the negative slope is more pronounced than for a thick conductor $(t = 3.\mu\text{m})$ and the losses are visibly higher.

Besides the conductor losses the backmetallization losses in a CPW may contribute significantly to the overall losses in particular when a single layer of thin substrate is used. From the previous discussion it is clear that for 10 mils substrate thickness a relatively strong E-field can exist between the center conductor and the backmetallization and that this E-field is naturally concentrated below the center conductor. The polarization of this field can either by vertical or horizontal (with respect to the groundplane), depending on the mode of operation. Therefore, one might expect that the overall losses depend to a degree also on the conductivity of the backmetallization. This is indeed true, but only if the substrate thickness is in the order of 50 μm or less. Fig. 9 illustrates the effect of different conductivity for the backmetallization. Also shown in this figure is the effect of an inhomogeneous backmetallization, that is one with a strip of different conductivity embedded into the backmetallization. Three different situations are illustrated: a) lossless backmetallization, b) lossy backmetallization with a homogeneous skin-effect layer (low density copper, $\sigma_g = 2.53 \times 10^4\,(\Omega\,\text{mm})^{-1}$), and c) a highly conductive strip embedded into the groundplane (high density copper strip, $\sigma_g = 5.78 \times 10^4\,(\Omega\,\text{mm})^{-1}$). The first observation is that the thin film structure is more dispersive in all three cases compared to the 10 mils substrate. Secondly, in the case of a lossless backmetallization, the overall losses seem to have a peak value at about 30 GHz and tend to decrease for higher frequencies. This effect becomes less pronounced if the conductivity of the backmetallization decreases. For 10 mils alumina substrate the conductivity of the backmetallization has no visible effect on the overall losses and is therefore not shown. The highly conductive strip embedded in a backmetallization of lower

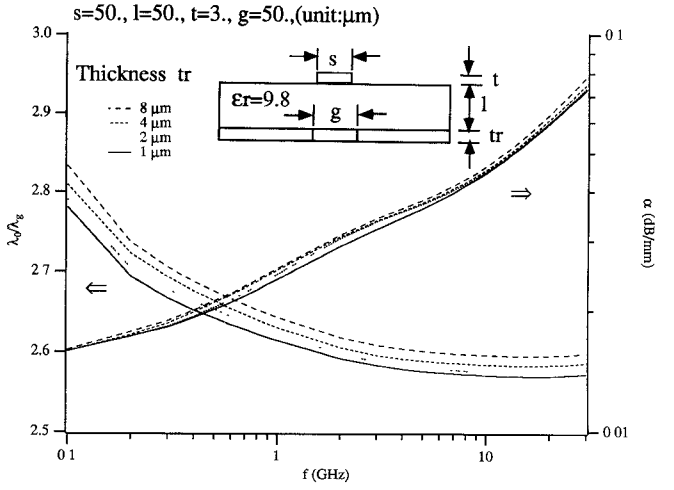

Fig. 10. Comparison of dispersion and loss characteristic of microstrip lines on very thin substrate with a resistive strip of different thickness embedded into the groundplane. The groundplane consist of high density copper $(5.98 \times 10^{4}\,\Omega\,\mathrm{mm})^{-1}$. The conductor is assumed to be gold.

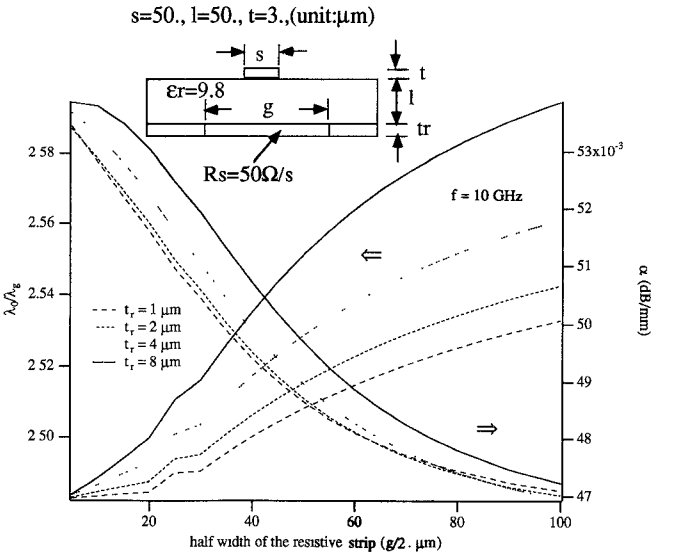

Fig. 11. Effect of the half-width of the resistive strip on losses and propagation constant of the microstrip line of Fig. 10.

conductivity does not seem to influence the loss characteristics of the CPW significantly. However, if this strip is assumed to be resistive and embedded in the groundplane of a microstrip line, its effect is significant and could be used to design integrated planar attenuators.

Fig. 10 shows the dispersion behaviour of the microstrip line on 50 μm thin alumina substrate with a resistive strip embedded in the groundplane. Both, the conductor width (s) and (groundplane) strip width (g) equal 50 μm. Although the substrate thickness is unusual for alumina, it is used here to be consistent with the transmission line parameters in the previous part of this investigation. Substituting GaAs for alumina results qualitatively in the same characteristics. As illustrated in Fig. 10, slight variations in the strip thickness have only a marginal effect on the overall losses but result in visible changes of the propagation constant. Increasing the width (g) of the resistive strip increases the propagation constant but lowers the overall losses. This effect is shown in Fig. 11. Fig. 12 illustrates the effect of different material resistivity and thickness of the strip $(s = g = 50\,\mu\mathrm{m})$. It is interesting to see that the propagation constant increases with the strip thickness up to approximately $tr = 100\,\mu$m and then decreases slightly, but that the overall losses increase exponentially $(Rs = 100\,\Omega/\mathrm{sq})$.

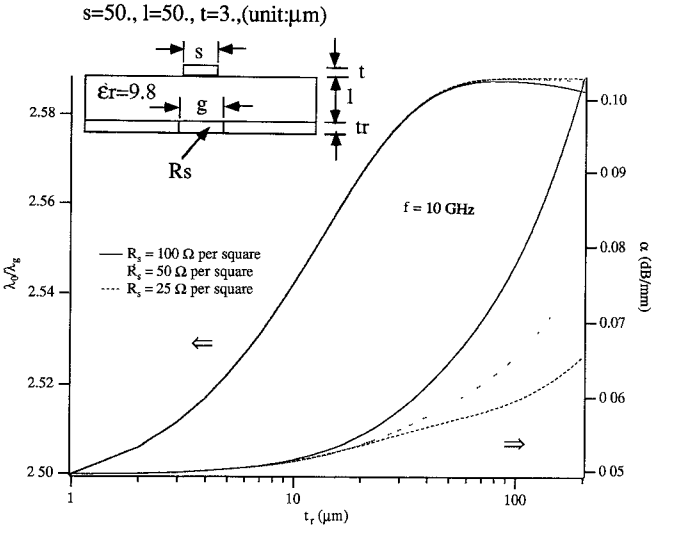

Fig. 12. Effect of the resistivity of the groundplane strip on the loss and propagation constant of the microstrip line of Fig. 10.

IV. Conclusion

This paper has presented a rigorous analysis of thin-film CPW and microstrip transmission lines taking into account the metallic losses of all conductors including the groundplane and backmetallization. It was shown that the fundamental mode in a CPW with lossy conductors and backmetallization can have a relatively strong E-field concentration between the center conductor and the backmetallization and that the field distribution significantly deviates from that of the classical CPW mode. Furthermore, at low frequencies the fundamental mode shows a negative slope of the propagation constant, which was also observed for a thin-film microstrip line at frequencies up to 20 GHz. It was demonstrated that the conductivity of the CPW backmetallization may be an important loss factor when very thin substrate material is used. The effect of a resistive strip in the groundplane of a microstrip line has been investigated and may be useful for the design of planar attenuators.

Appendix

As shown in [21], the best choice of discretizing a structure is such that a ψ^h-potential line coincides with the interface line. Furthermore, for equidistant discretization the value of ϵ^h at interfaces where the dielectric constant changes abruptly, should take the arithmetic mean of the two adjacent ϵ_r values. For non-equidistant discretization, however, it is not readily apparent which value of ϵ_r is to be inserted in $[\epsilon^h]$ along the interface line. To answer this question, a similar analytical derivation to [21] is made in this section. With reference to Fig. 2, the tangential E-field and the normal H-field components

to this interface should be continuous:

$$\begin{aligned} \psi_G^1 &= \psi_G^2 \\ \frac{1}{\epsilon_{r1}}\frac{\partial \psi_G^1}{\partial x} &= \frac{1}{\epsilon_{r2}}\frac{\partial \psi_G^2}{\partial x} \end{aligned} \tag{A1}$$

in addition,

$$\begin{cases} \psi_{k+1}^1 \approx \psi_G + \dfrac{d\psi^1}{dx}h_2 \\ \psi_{k+1}^2 \approx \psi_G + \dfrac{d\psi^2}{dx}h_2 \end{cases} \tag{A2}$$

$$\begin{cases} \psi_k^1 \approx \psi_G - \dfrac{d\psi^1}{dx}h_1 \\ \psi_k^2 \approx \psi_G - \dfrac{d\psi^2}{dx}h_1 \end{cases} \tag{A2}$$

Combining the first order approximation (A2), (A3) with (A1) leads to

$$\begin{cases} h_1\dfrac{d\psi^1}{dx} = \dfrac{\epsilon_{r1}h_1}{\epsilon_{r1}h_1 + \epsilon_{r2}h_2}(\psi_{k+1} - \psi_k) \\ h_2\dfrac{d\psi^2}{dx} = \dfrac{\epsilon_{r2}h_2}{\epsilon_{r1}h_1 + \epsilon_{r2}h_2}(\psi_{k+1} - \psi_k) \end{cases} \tag{A4}$$

Along line k the relationship in (A5) at the bottom of the page exists. From the analytical expression (A5) and (A6) the equivalent dielectric constant can then be derived from the generalized cases:

$$\begin{aligned} \epsilon_G = \epsilon_r^h|_{\text{interface}} &= \frac{\epsilon_{r2}h_2 + \epsilon_{r1}h_1}{h_1 + h_2} \\ &= \epsilon_{r2} + (\epsilon_{r1} - \epsilon_{r2})\kappa \\ \kappa &= \frac{h_1}{h_1 + h_2} \quad \text{with} \quad 0 < \kappa < 1 \end{aligned} \tag{A7}$$

ACKNOWLEDGMENT

This work was financiallyl supported by a grant from MPR Teltech, vancouver, and the National Science and Engineering Research Council of Canada (NSERC).

REFERENCES

[1] R. H. Jansen, "A novel CAD tool and concept compatible with the requirements of multilayer GaAs MMIC Technology," in *IEEE MTT-S Int. Microwave Symp. Dig.* St. Louis, 1985, pp. 711–714.

[2] H. A. Wheeler, "Formulas for the skin effect," *Proc. IRE,* vol. 30, pp. 412–442, 1942.

[3] R. A. Pucel, D. J. Masse, and C. P. Hartwig, "Losses in microstrip," *IEEE Trans. Microwave Theory Tech.,* vol. MTT-16, June 1968.

[4] Z. Pantic-Tanner and R. Mittra, "Finite-element matrices for loss calculation in quasi-TEM analysis of microwave transmission lines," *Microwave and Optical Technology Lett.,* vol. 1, no. 4, pp. 142–146.

[5] R. Pregla, "Determination of conductor losses in planar waveguide structures," *IEEE Trans. Microwave Theory Tech.,* vol. MTT-28, pp. 433–434, 1980.

$$\begin{aligned} \frac{d}{dx}\left(\frac{1}{\epsilon_{r1}}\frac{d\psi}{dx}\right) &= \frac{\dfrac{\psi_{k+1} - \psi_k}{\epsilon_{r1}h_1 + \epsilon_{r2}h_2} - \dfrac{\psi_k - \psi_{k-1}}{\epsilon_{r1}h_{i-1}}}{e_{i-1}} \\ &= \frac{\psi_{k-1}}{\epsilon_{r1}e_{i-1}h_{i-1}} \\ &\quad - \left(\frac{1}{\epsilon_{r1}e_{i-1}h_{i-1}} + \frac{1}{e_{i-1}h_{i-1}\left(\epsilon_{r2} + \dfrac{\epsilon_{r1} - \epsilon_{r2})h_1}{h_i}\right)}\right)\psi_k \\ &\quad + \frac{\psi_{k+1}}{e_{i-1}h_i\left(\epsilon_{r2} + \dfrac{(\epsilon_{r1} - \epsilon_{r2})h_1}{h_i}\right)} \end{aligned} \tag{A5}$$

Similarly, along line $k + 1$:

$$\begin{aligned} \frac{d}{dx}\left(\frac{1}{\epsilon_{r1}}\frac{d\psi}{dx}\right) &= \frac{\dfrac{\psi_{k+2} - \psi_{k+1}}{\epsilon_{r2}h_{i+1}} - \dfrac{\psi_{k+1} - \psi_k}{\epsilon_{r1}h_1 + \epsilon_{r2}h_2}}{e_i} \\ &= \frac{\psi_k}{e_ih_i\left(\epsilon_{r2} + \dfrac{(\epsilon_{r1} - \epsilon_{r2})h_1}{h_i}\right)} \\ &\quad - \left(\frac{1}{\epsilon_{r2}e_ih_{i+1}} + \frac{1}{e_ih_i\left(\epsilon_{r2} + \dfrac{\epsilon_{r1} - \epsilon_{r2})h_1}{h_i}\right)}\right)\psi_{k+1} \\ &\quad + \frac{\psi_{k+2}}{\epsilon_{r2}e_ih_{i+1}} \end{aligned} \tag{A6}$$

[6] H. J. Finlay, R. H. Jansen, J. A. Jenkins, and I. G. Eddison, "Accurate characterization and modelling of transmission lines for GaAs MMIC's," *IEEE Trans. Microwave Theory Tech.*, vol. 36, pp. 961–967, June 1988.
[7] D. Mirshekar-Syahkal and J. B. Davies, "Accurate solution of microstrip and coplanar structures for dispersion and for dielectric and conductor losses," *IEEE Trans. Microwave Theory Tech.*, vol. MTT-27, no. 7, pp. 694–699, July 1979.
[8] T. E. Van Deventer, P. B. Katehi, and A. C. Cangellaris, "High frequency conductor and dielectric losses in shielded microstrip," in *1989 IEEE MTT-S Int. Microwave Symp. Dig.*, Long Beach, pp. 919–922.
[9] H. Y. Lee and T. Itoh, "Wideband conductor loss calculation of planar quasi-TEM transmission lines with thin conductors using a phenomenological loss equivalence method," in *1989 IEEE MTT-S Int. Microwave Symp. Dig.*, Long Beach, pp. 367–370.
[10] G. Costache, "Finite element method applied to skin-effect problems in strip transmission lines," *IEEE Trans. Microwave Theory Tech.*, vol. MTT-35, pp. 1009–1013, Nov. 1987.
[11] P. Waldow and I. Wolff, "The skin effect at high frequencies," *IEEE Trans. Microwave Theory Tech.*, vol. MTT-33, pp. 1076–1081, Oct. 1985.
[12] A. C. Cangellaris, "The importance of skin-effect in microstrip lines at high frequencies," in *IEEE MTT-S Int. Microwave Symp. Dig.*, New York, May 1988, pp. 197–198.
[13] W. Heinrich, "Full-wave analysis of conductor losses on MMIC transmission lines," in *IEEE MTT-S Int. Microwave Symp. Dig.*, Long Beach, May 1989, pp. 911–914.
[14] ——, "Full-wave analysis of conductor losses on MMIC transmission lines," *IEEE Trans. Microwave Theory Tech.*, vol. 38, pp. 1468–1472, Oct. 1990.
[15] K. Wu and R. Vahldieck, "A self-consistent approach to determine loss properties in MIC/MMIC coplanar transmission lines," in *Proc. 3rd Asia-Pacific Microwave Conf.*, paper 35-4, Tokyo, Sept. 18–21, 1990, pp. 823–826.
[16] F. J. Schm\"uckle and R. Pregla, "The method of lines for the analysis of lossy waveguides," *IEEE Trans. Microwave Theory Tech.*, vol. 38, pp. 1473–1479, Oct. 1990.
[17] Y. C. Shih and M. Maher, "Characterization of conductor-backed coplanar waveguides using accurate on-wafer measurement techniques," in *1990 IEEE MTT-S Int. Microwave Symp. Dig.*, Dallas, pp. 1129–1132.
[18] T. Y. Hirota and H. Ogawa, "Uniplanar MMIC hybrids—a proposed new MMIC structure," *IEEE Trans. Microwave Theory Tech.*, vol. MTT-35, pp. 576–581, June 1987.
[19] V. Shulz and R. Pregla, "A new technique for the analysis of the dispersion characteristics of planar waveguides," *Arch. Elec. Übertragung.*, vol. 34, pp. 169–173, 1980.
[20] S. B. Worm and R. Pregla, "Hybrid-mode analysis of arbitrarily shaped planar microwave structures by the method of lines," *IEEE Trans. Microwave Theory Tech.*, vol. MTT-32, pp. 191–196, Feb. 1984.
[21] R. Pregla, M. Koch, and W. Pascher, "Analysis of hybrid waveguide structures consisting of microstrips and dielectric waveguides," in *Proc. 17th European Microwave Conf.*, Rome, pp. 927–932.
[22] R. E. Collin, *Field Theory of Guided Waves*. New York: McGraw-Hill, 1960, pp. 224–234.
[23] H. Diestel and S. B. Worm, "Analysis of hybrid field problems by the method of lines with nonequidistant discretization," *IEEE Trans. Microwave Theory Tech.*, vol. MTT-32, pp. 633–638, June 1984.

Ke Wu (M'87) was born in Jiangsu, China, on December 9, 1962. He received the B.Sc. degree (with distinction) in radio engineering from Nanjing Institute of Technology (Now Southeast University), Nanjing, China, in 1982 and the D.E.A. degree in electronics and Ph.D. degree (with distinction) in optics, optoelectronics, and microwave engineering from the Institut National Polytechnique de Grenoble (INPG), Grenoble, France, in 1984 and 1987, respectively.

During the years 1983–1987, he conducted research in the Laboratoire d'El\'ectromagnetisme, Microondes et Optiques guid\'es (LEMO), Grenoble, France. From 1988 to 1992 he was a research associate in the Department of Electrical and Computer Engineering at the University of Victoria, Victoria, B.C., Canada. Since 1992 he has been with "Groupe de Recherches Avanc\'ees Microondes et Electroniques Spatiales (POLY-GRAMES)" at the Ecole Polytechnique de Montr\'eal, PQ, Canada, where he is an assistant professor in the Department of Electrical and Computer Engineering. His main research interests include electromagnetic fields, numerical methods, analysis and design of various microwave/millimeter-wave integrated and monolithic circuits, electro-optic and optoelectronic components, lightwave transmission systems, planar antennas and microwave/optical signal processing.

Dr. Wu received a Chinese Overseas Graduate Fellowship in 1982, a U. R. S. I. Young Scientist Award in 1987, and, together with two coauthors, the Oliver Lodge Premium from the IEE for the outstanding publication in 1988.

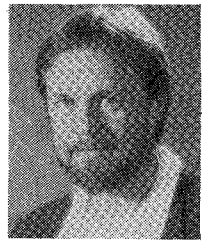

Rüdiger Vahldieck (M'85–SM'86) received the Dipl.-Ing. and the Dr.-Ing. degrees in electrical engineering from the University of Bremen, West Germany, in 1980 and 1983, respectively.

From 1984 to 1986 he was a Research Associate at the University of Ottawa, Canada. In 1986 he joined the University of Victoria, British Columbia, Canada, where he is now a Full-Professor in the Department of Electrical and Computer Engineering. His research interest include numerical methods to model electromagnetic fields for computer-aided design of microwave, millimeter wave and opto-electronic integrated circuits. He is interested in design aspects of passive and active planar and quasi-planar components and filters for MMIC and MHMIC applications. Recently he has been involved in research on subcarrier multiplexed lightwave systems. The emphasis of this work is on broad bandwidth electro-optic modulators and on coherent detection systems in fiber-optic communication links.

Dr. Vahldieck, together with three coauthors, received the outstanding publication award of the Institution of Electronic and Radio Engineers in 1983. He is on the editorial board of IEEE TRANSACTIONS ON MICROWAVE THEORY AND TECHNIQUES and he has published more than 80 technical papers in the field of microwave CAD.

Josef L. Fikart (S'70–M'72–SM'86) was born in Czechoslovakia on April 3, 1939. He received the Ing. degree (M.Sc.) in electrical engineering from the Czech Technical University in Prague in 1966 and the Ph.D. degree, also in electrical engineering, from the University of Alberta in Edmonton in 1973. The subject of his doctoral thesis was large-signal treatment of IMPATT oscillator noise.

Prior to his Ph.D. studies, he worked as a microwave research engineer on varactor amplifiers and multipliers at the Radio Engineering Institute of the Czechoslovak Academy of Science. Since 1973, Dr. Fikart has been associated with MPR Teltech Ltd. (formerly GTE Lenkurt Electric - Canada) in Vancouver, BC, working on the development of microwave subsystems for microwave radio, satellite earth stations and other applications. He is now Technical Specialist and Manager, Microwave Development, overseeing a wide range of design activities including the development of MMICs, as well as MHMICs and uniplanar structures at EHF. Since 1984, he has also been associated with the University of British Columbia as a Lecturer and Adjunct Professor.

Dr. Fikart published over 20 papers, and received 5 patents, in the area of microwave electronics.

E. (Hector) Minkus received the Engineering Diploma in electronics and telecommunications from the Enrico Fermi Institute of Technology in Rome, Italy in 1958.

Currently, he is the Program Manager of the Miniature Hybrid Microwave Integrated Circuit Project at MPR Teltech Ltd./Burnaby, BC, Canada. Previously, he worked with Selenia Spa/Italy, DECCA RADAR/Toronto and Communications Research Centre/Ottawa, Canada. He was involved in designing military, space and commercial microwave systems and subsystems.